Image Resolution Enhancement and its applications to Medical Image Processing

Shantanu H. Joshi[1], Antonio Marquina[2,3], Stanley J. Osher[3], Ivo Dinov[1], John Darrell Van Horn[1], and Arthur Toga[1]

[1] Laboratory of Neuroimaging, University of California, Los Angeles, CA 90095, USA
[2] Departamento de Matematica Aplicada, Universidad de Valencia, C/ Dr Moliner, 50, 46100 Burjassot, Spain
[3] Department of Mathematics, University of California, Los Angeles, CA 90095, USA

Abstract. This paper focuses on a new image resolution enhancement method based on the TV regularization model by Marquina and Osher. The low resolution images considered in this paper are natural images as well as 3D anatomical MRI scans of patients. The idea of image resolution enhancement concerns with the improvement of image resolution based on the fusion of several acquisitions of low resolution observations by the imaging sensor. We also demonstrate the coarse to fine effect of the Bregman iterative procedure that helps to recover finer scales from the reconstructed image. Additionally, we propose a new edge-preserving up (down) sampling operator that yields a significant improvement during the up/down sampling stage of the method.

Keywords: Edge-preserving operators, total variation regularization, deconvolution, Gaussian blur, Bregman iteration, up/down sampling

1 Introduction

With the recent advances in low-cost imaging solutions and increasing storage capacities, there is an increased demand for better image quality in a wide variety of applications involving both image and video processing. While it is preferable to acquire image data at a higher resolution to begin with, one can imagine a wide range of scenarios where it is technically not feasible. In some cases, it is the limitation of the sensor due to low-power requirements as in satellite imaging, remote sensing, and surveillance imaging. In other cases, it is the limitation of the sensed environment itself, for e.g. the presence of atmospheric clutter, background noise, unfavorable weather , etc., etc. In some cases, it is a combination of both, for e.g. the acquisition of medical images is limited both by the physical issues of MRI imaging, as well as the time constraints of subjecting the magnetic field to patients without becoming a health hazard. One measurement of image quality is the spatial resolution of the pixels distributed per unit length/area. An improvement in the spatial resolution for still images directly improves the ability to discern important features in images with a better precision.

The low-resolution data can exist in the form of still images, a sequence of image frames devoid of inter-frame motion, a single video sequence, or a collection of video sequences. Furthermore the observations can be corrupted by motion-induced artifacts either in the case of still images or videos. The collective approach that tackles

the problem of reconstructing a high-resolution image from one or more of the above low-resolution observations is termed as super-resolution. There are several prominent approaches to this problem, all of them largely employing various cues such as sub-pixel shifts between successive frames, the camera blur, defocus, and zoom , etc. These approaches can be divided into two types, one that uses motion information between successive frames (e.g., video super-resolution), and the other that uses a motion-free approach. Most of these approaches usually expect multiple low-resolution observations as input. Super-resolution image reconstruction is an ill-conditioned inverse problem, since the observation process of the original high resolution object consists of a noisy blurred low resolution observation affected by sampling artifacts, blurring and noise. This is mathematically modeled as a nonlinear process consisting of a convolution operator acting on the image, followed by a down sampling operation and the mixing of additive noise. Most of the earlier research work has been developed in the frequency domain approach using (discrete) Fourier transform and wavelet-transform based methods. For e.g. the approach of Tsai and Huang [20] first outlined the idea of super-resolution in their seminal paper. Peleg *et al.* [8] used the iterative back projection scheme to achieve image reconstruction. Yet another approach [19] uses projections on convex sets (POCS) of images to restrict the solution domain for reconstruction. A hybrid approach by Elad and Feuer [5] combines the POCS and the maximum likelihood approaches for both motion-based and motion-free super-resolution. A very different set of methods use the learning-based approach for super-resolution. The general idea here is to learn a set of image features from exemplar images and use them for the reconstruction of a high-resolution image. Capel and Zisserman [2] use PCA on face image databases to learn the image model and use it to reconstruct images from multiple views. Freeman *et al.* [6] learn a feature set of image patches that encode the relationships among different spatial frequencies from a large training set and use it as prior information for reconstructing higher frequencies for resolution enhancement. The reader is referred to an excellent monograph by Chaudhari and Joshi [4] for a comprehensive bibliography and references in the field. Along with a wide range of applications of super-resolution methods in tasks such as satellite image processing, surveillance, computer vision, and even video processing, there has been a considerable effort by researchers trying to apply these methods to medical imaging. In particular, MRI acquisitions usually have a low-resolution in the inter-slice direction, and it is of considerable interest to "fill-in" the intermediate slices. Carmi *et al.* [3] use sub-pixel shifted MR (Magnetic Resonance) images for high resolution reconstruction. Greenspan *et al.* [7] combine several low resolution images in the slice-select direction to achieve SR reconstruction. Kornprobst *et al.* [9] also achieve higher resolution in the slice-select direction for fMRI sequences.

While super-resolution methods attempt to exploit the information redundancy in several low-resolution observations of images, at times, only a single low-resolution instance of the image is available. This is sometimes the case in MRI images, where due to economic or health reasons, a patient is scanned only once over a period of time, or the time elapsed between successive scans may be too large to preserve any temporal coherence to take advantage of. This is the idea that is explored in this paper, where we will focus mainly on the problem of single frame high resolution reconstruction of images. A super-resolution related variational model using the total variation (TV) norm as regularizing functional for de-blurring and oversampling a single noisy image was also proposed in [10] . This model was formulated and solved in the Fourier domain

assuming periodic boundary conditions by means of the gradient descent method and using characteristic functions as convolution kernels.

Our approach will be based upon a variational model that uses the TV norm [15] as a regularizing functional. Recently, Marquina *et al.* [12] have proposed a new variational model based on the TV norm [15] for super-resolution of multidimensional images. They use a new multi-scale approach (Bregman iterations) for iterative refinement and recovery of finer details in images. We will follow this approach to solve the more general super-resolution problem using the TV norm as regularizing functional. The proposed model uses a multi-frame dataset instead of a single image and Gaussian kernels of convolution allowing homogeneous Neumann boundary conditions. In addition, we propose an iterative refinement procedure based on an original idea by Bregman [1], as suggested and implemented in [11], to improve spatial resolution. The proposed super-resolution method improves the behavior of any interpolation method (including high order and sinc interpolation) because our method preserves edges satisfactorily avoiding Gibbs phenomenon and the iterative refinement procedure allows us to recover fine scales of the image.

This paper is organized as follows: Section 2 outlines the super-resolution model using TV regularization. In particular, it explains the variational model as well as a new scale-space approach that utilizes the Bregman iterative procedure for recovering finer details from images. Additionally, section 2.2 proposes a new edge-preserving up (down) sampling operator used in the model. Section 3 presents details of the numerical implementation of the model. Section 4 demonstrates experimental results for a few 2D natural images as well as 2D slices and 3D volumes of MRI images, followed by the summary.

2 Image Observation and Synthesis Model

The low resolution image observation model can be formulated in a standard fashion as a down-sampled degraded version of the original high resolution image. We assume that the low resolution image f is defined on a subset of a plane $\Omega \subset \mathbb{R}^k$. For the purpose of this paper, k is either 2 or 3. Here onwards, all the notation will be specified for $3D$ images. The restriction to $2D$ images is straightforward. For a discrete representation, we assume $f \in \mathbb{R}^n \times \mathbb{R}^m \times \mathbb{R}^p$. Let the unknown high resolution image to be estimated be given by $u \in \mathbb{R}^{2m} \times \mathbb{R}^{2n} \times \mathbb{R}^{2p}$. Then given a linear down sampling operator D, we can write the observation model as,

$$f = D(h * u) + n, \tag{1}$$

where n is an additive Gaussian white noise with zero mean and variance σ^2, and h is translation invariant convolution kernel corresponding to the point spread function of the imaging device. A related problem in the above formulation is the estimation of the kernel h, that we shall skip in this paper. Throughout this paper, we assume that the kernel is given by the Gaussian,

$$h(x, y, z) = Ke^{-\frac{1}{2}\left[\frac{x^2}{\sigma_x^2}+\frac{y^2}{\sigma_y^2}+\frac{z^2}{\sigma_z^2}\right]}, \tag{2}$$

where K is a normalization constant, and $\sigma_x, \sigma_y, \sigma_z$ are variances along the X, Y, and Z directions respectively. The problem in Eqn. 1 is usually solved as a constrained op-

timization problem that seeks to minimize the regularizer $\int_\Omega ||\nabla u||^2 dxdy$, while constraining the noise to be $||h * u - f||^2_{\mathbb{L}^2} = \sigma^2$. This ensures that the reconstructed image u is free of discontinuities. However in order to recover the edges satisfactorily, Rudin and Osher [15] propose the total variation norm as the regularizing functional. The total variation norm is given as,

$$\text{TV}(u) = \int_\Omega |\nabla u| dxdy \tag{3}$$

Using the regularizer in Eqn. 3, we can state the single frame image reconstruction model as the minimization problem as follows:

$$\hat{u} = \underset{u}{\text{argmin}}\{TV(u) + \frac{\lambda}{2}[||f - D(h * u)||^2_{\mathbb{L}^2} - \sigma^2]\} \tag{4}$$

The Euler-Lagrange formulation for Eqn. 4 can be written as

$$\nabla \cdot \frac{\nabla u}{|\nabla u|} + \lambda(\tilde{h} * S(f) - \tilde{h} * (S \circ D(h * u))) = 0 \tag{5}$$

$$\implies \nabla \cdot \frac{\nabla u}{|\nabla u|} + \lambda \tilde{h} * (\bar{g} - T(h * u)) = 0 \tag{6}$$

where $\bar{g} = S(f)$, and the operator T is defined as $T = S \circ D$.

The Euler-Lagrange equation given by Eqn. 6 can be solved as a time-dependent equation

$$u_t = \nabla \cdot \frac{\nabla}{|\nabla u|} + \lambda \tilde{h} * (\bar{g} - T(h * u)) \tag{7}$$

with homogeneous Neumann boundary conditions and initiating with $u_0 = S(f)$.

2.1 Bregman Iterative Method

The convergence of Eqn. 7 to the steady state yields a reconstructed high resolution image. However if one wishes to recover even finer scales from the reconstructed image, one can use the Bregman iterative refinement procedure [1] to do so. If u_0 is the solution of Euler-Lagrange equation (6), then we have,

$$\nabla \cdot \frac{\nabla u_0}{|\nabla u_0|} + \lambda \tilde{h} * (\bar{g} - T(h * u_0)) = 0 \tag{8}$$

We will denote the image residual in the high resolution scale by v_0 as,

$$v_0 = \bar{g} - T(h * u_0) \tag{9}$$

We now solve the Euler-Lagrange equation for the new image $\bar{g} + v_0$ to obtain a new solution, which we denote by u_1. Again, the solution u_1 will satisfy

$$\nabla \cdot \frac{\nabla u_1}{|\nabla u_1|} + \lambda \tilde{h} * \Big(\bar{g} + v_0 - T(h * u_1)\Big) = 0, \tag{10}$$

where the new residual is defined as

$$v_1 = \bar{g} + v_0 - T(h * u_1) \tag{11}$$

and so on. We term the sequence of images $u_0, u_1, \cdots, u_j, \cdots$ as Bregman iterates. It is advisable to terminate this procedure when a satisfactory image quality is obtained, otherwise it has a tendency to recover noise after all the finer scales in the image are recovered. This iterative procedure was introduced for image restoration in [14] and has also been used for blind deconvolution of images based on TV norm in [11].

2.2 Edge-preserving Up (Down)-sampling operator

There are various choices for the up (S) and down (D) sampling operators used in the observation model in Eqn. 1 and the synthesis model in Eqn. 6 respectively. The simplest down sampling operator can be an averaging operator that simply averages the eight neighbors of the pixel using either a Gaussian kernel, or an arithmetic average. Equivalently, the up sampling operation corresponding to the down sampling operator above simply involves repeating voxel values for each row, column, and slice. Alternately, one can also use 3D bilinear interpolation for up sampling and down sampling images. The problems with the above approaches are the unnecessary blurring (averaging) that is caused at each step of the iteration while solving the Euler Lagrange equation in 6. To overcome this problem, one can further suggest the use of better signal preserving operators that use sinc or Fourier interpolation for up and down sampling. However these methods can potentially introduce ringing artifacts in images with sharp edges or boundaries.

Especially for images with prominent edges and interfaces, we need an appropriate interpolation operator that preserves these features. Accordingly, we propose a new piecewise-linear up (down) sampling operator that preserves such edges and boundaries. We describe the edge-preserving operator in detail below.

We set up the grid $x_j = (j-1)\Delta x, y_k = (k-1)\Delta y$ and $z_l = (l-1)\Delta z$, where $\Delta x > 0, \Delta y > 0, \Delta z > 0$ and $j = 1, \ldots, n, k = 1, \ldots, m$ and $l = 1, \ldots, p$. We define the domain $E = [0, A] \times [0, B] \times [0, C]$, where $A = (n-1)\Delta x$, $B = (n-1)\Delta y$, and $C = (n-1)\Delta z$. We consider the grid function u defined as

$$u_{j,k,l} : \mathbb{R}^3 \rightarrow \mathbb{R}^3$$

We define the **edge-preserving piecewise linear approximation** of the grid function u as the function $L(x, y, z)|_{E_{jkl}} = L_{jkl}(x, y, z)$ where the computational voxel E_{jkl} is given by

$$E_{jkl} = [x_j - \frac{\Delta x}{2}, x_j + \frac{\Delta x}{2}] \times [y_k - \frac{\Delta y}{2}, y_k + \frac{\Delta y}{2}] \times [z_l - \frac{\Delta z}{2}, z_l + \frac{\Delta z}{2}]$$

and

$$L_{jkl}(x, y, z) = u_{j,k,l} + a(x - x_j) + b(y - y_k) + c(z - z_l),$$

where a, b, and c are determined from

$$a = \text{minmod}\left(\frac{\Delta_-^x u_{j,k,l}}{\Delta x}, \frac{\Delta_+^x u_{j,k,l}}{\Delta x}\right) \tag{12}$$

$$b = \text{minmod}\left(\frac{\Delta_-^y u_{j,k,l}}{\Delta y}, \frac{\Delta_+^y u_{j,k,l}}{\Delta y}\right) \tag{13}$$

$$c = \text{minmod}\left(\frac{\Delta_-^z u_{j,k,l}}{\Delta z}, \frac{\Delta_+^z u_{j,k,l}}{\Delta z}\right), \tag{14}$$

where the operations in the term containing derivatives are understood component-wise, and

$$\begin{aligned} \Delta_{\pm}^{x} u_{i,j,k}^{n} &= \pm(u_{i\pm1,j,k}^{n} - u_{i,j,k}^{n}) \\ \Delta_{\pm}^{y} u_{i,j,k}^{n} &= \pm(u_{i,j\pm1,k}^{n} - u_{i,j,k}^{n}) \\ \Delta_{\pm}^{z} u_{i,j,k}^{n} &= \pm(u_{i,j,k\pm1}^{n} - u_{i,j,k}^{n}), \end{aligned} \tag{15}$$

where i, j, k are the indices of the 3D grid.

The minmod(d, e) function is defined as,

$$\text{minmod}(d, e) = \frac{\text{sgn}(d) + \text{sgn}(e)}{2} \min(|d|, |e|), \tag{16}$$

where sgn$(d) = 1$ if $d \geq 0$ and sgn$(d) = -1$ otherwise.

The function $L_{jkl}(x, y, z)$ is defined on the computational voxel E_{jkl}. We want to up-(down) sample the grid function u with a spatial resolution of $h_x > 0, h_y > 0, h_z > 0$. Then the up-(down) sampled grid function v is defined on a new grid $v(q, r, s)$ for $q = q, \ldots, nh, r = 1, \ldots, mh$, and $s = 1 \ldots, ph$ where

$$\begin{aligned} nh &= \text{floor}\left(\frac{A}{h_x}\right) \\ mh &= \text{floor}\left(\frac{B}{h_y}\right) \\ ph &= \text{floor}\left(\frac{C}{h_z}\right), \end{aligned}$$

where floor(d) is the maximum of all integers i such that $i \leq d$. The new grid is then defined as $x_{h_q} = (q-1)h_x, y_{h_r} = (r-1)h_y$, and $z_{h_s} = (s-1)h_z$. Based on this grid, the function v is defined as $v(q, r, s) = L(x_{h_q}, y_{h_r}, z_{h_s})$.

We demonstrate the edge-preserving property of the above operator by applying it to a checkerboard pattern as shown in Fig. 1. Figure 1 shows a low-resolution image, as well as its up sampled versions using a bilinear, sinc and the edge-preserving operator for two different types of checkerboard patterns. It also shows a magnified portion from the center of the image. It is noticed that the bilinear and the sinc interpolation operators introduce significant spurious levels of gray in between the black squares in the pattern. Furthermore, they have a tendency to smooth out the boundaries of the flat black squares in the image. In contrast, the edge-preserving operator has retained, and in some cases even enhanced the boundaries and edges as compared to the low-resolution image.

3 Numerical Implementation

This section discusses the numerical implementations of the solution to the Euler Lagrange equation. The Euler-Lagrange derivative of the TV-norm is not well defined at points where $\nabla u = 0$, due to the presence of the term $\frac{1}{|\nabla u|}$. Hence we modify the regularization TV functional as follows:

$$\int_{\Omega} \sqrt{|\nabla u|^2 + \epsilon}\, dxdy \tag{17}$$

where ϵ is a small positive parameter or

$$\int_{\Omega} |\nabla u|_{\epsilon} \, dxdy \tag{18}$$

with the notation

$$|v|_{\epsilon} = \sqrt{|v|^2 + \epsilon} \tag{19}$$

for $v \in R^2$.

We express the 3D model (7) in terms of explicit partial derivatives

$$\begin{aligned} u_t =& \lambda \tilde{h} * (\bar{g} - T(h * u)) \\ &+ \frac{u^n_{xx}((u^n_y)^2 + (u^n_z)^2 + \epsilon)) + u^n_{yy}((u^n_x)^2 + (u^n_z)^2 + \epsilon)) + u^n_{zz}((u^n_x)^2 + (u^n_y)^2 + \epsilon))}{[(u^n_x)^2 + (u^n_y)^2 + (u^n_z)^2 + \epsilon]^{3/2}} \\ &+ \frac{-2u^n_{xy}u^n_x u^n_y - 2u^n_{xz}u^n_x u^n_z - 2u^n_{yz}u^n_y u^n_z}{[(u^n_x)^2 + (u^n_y)^2 + (u^n_z)^2 + \epsilon]^{3/2}} \end{aligned} \tag{20}$$

using $u_0 = S(f)$ as the initial guess and homogeneous Neumann boundary conditions (i.e. absorbing boundary).

The above expression can also be rewritten as

$$\begin{aligned} \frac{u^{n+1}_{i,j,k} - u^n_{i,j,k}}{\Delta t} &= \lambda[\tilde{h} * (\bar{g} - T(h * u^n))]_{i,j,k} \\ + \frac{u^n_{xx}((u^n_y)^2 + (u^n_z)^2 + \epsilon)) + u^n_{yy}((u^n_x)^2 + (u^n_z)^2 + \epsilon)) + u^n_{zz}((u^n_x)^2 + (u^n_y)^2 + \epsilon))}{[(u^n_x)^2 + (u^n_y)^2 + (u^n_z)^2 + \epsilon]^{3/2}} & \\ + \frac{-2u^n_{xy}u^n_x u^n_y - 2u^n_{xz}u^n_x u^n_z - 2u^n_{yz}u^n_y u^n_z}{[(u^n_x)^2 + (u^n_y)^2 + (u^n_z)^2 + \epsilon]^{3/2}} & \end{aligned} \tag{21}$$

The approximations to the derivatives in Eqn. 21 can be calculated as:

$$\begin{aligned} [u^n_{xx}]_{i,j,k} &= \Delta^x_+ \Delta^x_- u^n_{i,j,k}/h^2_x \\ [u^n_{yy}]_{i,j,k} &= \Delta^y_+ \Delta^y_- u^n_{i,j,k}/h^2_y \\ [u^n_{zz}]_{i,j,k} &= \Delta^z_+ \Delta^z_- u^n_{i,j,k}/h^2_z \\ [u^n_{xy}]_{i,j,k} &= (\Delta^x_- + \Delta^x_+)(\Delta^y_- + \Delta^y_+)u^n_{i,j,k}/4(h_x h_y) \\ [u^n_{xz}]_{i,j,k} &= (\Delta^x_- + \Delta^x_+)(\Delta^z_- + \Delta^z_+)u^n_{i,j,k}/4(h_x h_z) \\ [u^n_{yz}]_{i,j,k} &= (\Delta^y_- + \Delta^y_+)(\Delta^z_- + \Delta^z_+)u^n_{i,j,k}/4(h_y h_z) \\ [u^n_x]_{i,j,k} &= (\Delta^x_- + \Delta^x_+)u^n_{i,j,k}/2h_x \\ [u^n_y]_{i,j,k} &= (\Delta^y_- + \Delta^y_+)u^n_{i,j,k}/2h_y \\ [u^n_z]_{i,j,k} &= (\Delta^z_- + \Delta^z_+)u^n_{i,j,k}/2h_z, \end{aligned} \tag{22}$$

where the derivatives along the x, y, and z direction are taken to be the same as defined in Eqn. 15. The Lagrange multiplier λ was chosen to be the maximum value for which the algorithm was stable. It was empirically determined to be $\lambda = 10$, and was not changed thereafter. The above algorithm was implemented in C++ using the FFTW library by Frigo and Johnson [13].

4 Experimental Results

Lastly, we demonstrate the algorithm by performing experiments with 2D natural images, 2D slices of 3D volumetric images, and finally the 3D volumetric MRI images.

4.1 Results for Natural Images

Figure 2 shows the results of the super-resolution reconstruction algorithm applied to a 380×285 map image. This image has been scaled to 760×570 by pixel-replication for display purposes. It can be observed that pixel replication inherently adds blocking artifacts to the image. The low-resolution image is up sampled by a factor of two using bilinear interpolation, and sinc interpolation, and finally using the super-resolution reconstruction method. It is noticed that the bilinear interpolation grossly smoothes out the image, the result due to sinc interpolation is somewhat better in the sense, some high frequency information is preserved. However the super-resolved reconstruction yields a sharp, crisp image, even resolving the little text at finer scales.

Figure 3 shows similar results with a 280×200 scene image. The first image in the top row shows the 560×400 pixel replicated image, whereas the last image is the super-resolved image. The bottom row shows a small portion of the image magnified to show detail. One can immediately observe the blocking effects due to pixel replication in the first image, and blurring of the edge boundaries in the bilinearly interpolated version. The edges get somewhat better using the sinc interpolation, but the best quality is given by the super-resolved image, that resolves and even enhances sharp edges and interfaces in the image. In both the above cases, we used an isotropic Gaussian kernel with kernel widths $\sigma_x = \sigma_y = 1$.

4.2 Results for 2D slices of 3D MRI image

In this experiment, we look at enhancing the in-plane resolution of individual transverse slices of a 3D MRI image. From left, all rows of Fig. 4 show an isotropic original image 180×216, the subsampled image, a Fourier interpolated image, and a super-resolved reconstructed image from the subsampled image. For display purposes, the subsampled image is shown at twice the resolution using pixel-replication. It is observed that the high resolved reconstructed image has sharper edge features, more details, and visually closely resembles the original image as compared to the Fourier interpolated result.

4.3 Results for full 3D MRI images

The proposed super-resolution algorithm can be applied to arbitrary 2D images or even 3D volumes of anisotropic voxel dimensions. In this experiment, we apply the reconstruction algorithm to the full 3D MRI image volume. Figure 5 shows a volume rendering of an original image of dimensions $256 \times 256 \times 160$, at voxel widths given by $1 \times 1 \times 1.25\, mm^3$. This image is first subsampled to half the resolution at $128 \times 128 \times 80$ ($2 \times 2 \times 2.5\, mm^3$) super-resolved to a full isotropic $256 \times 256 \times 160$ image with $1 \times 1 \times 1$ mm^3 resolution. As expected, we can see an improvement in the resolution plus an increase in the detail simultaneously across all X, Y, and Z dimensions. In this experiment, we used an anisotropic Gaussian kernel with the variances proportional to the voxel dimensions. Furthermore the grid dimensions for the edge-preserving up sampling and

down sampling operators were taken to be $\Delta x = \frac{h_x}{2}, \Delta y = \frac{h_y}{2}, \Delta z = \frac{h_z}{2}$, where h_x, h_y, h_z are the voxel dimensions of the appropriate up sampled or down sampled image.

4.4 Improving Results for Skull Stripping of MRI Brain Images

In this experiment we investigate the use of super-resolution as an enhancement pre-processing step for an important problem of skull stripping of brain MRI images. Whenever any patient undergoes a brain MRI scan, the resulting volumetric image always shows the skull cap, eye sockets, sometimes the cerebellum, or the brain stem. Often for diagnostic or even research purposes, the physician is only interested in looking at the brain tissue (comprising of the gray/white matter). For this purpose the MRI scan is processed to "skull-strip" unwanted anatomical features from the image. Currently, even though there are a wide variety of automated methods that perform skull stripping of MRI images, not all of them yield satisfactory results on a wide range of image data sets. Such methods often require manual intervention to fine tune the parameters of the algorithm.

We perform a comprehensive experiment using the LONI LPBA 40 data set [16]. The LONI Probabilistic Brain Atlas (LPBA40) is a series of maps of brain anatomic regions. These maps were produced from a set of whole-head MRI of 40 human volunteers. Each MRI is manually delineated to identify a set of 56 structures in the brain, most of which are within the cortex. These delineations are then transformed into a common atlas space to produce a set of co-registered anatomical labels. Additionally, the 3D volumes contained within this data set also represent intensity averages of the co-registered skull-stripped MRI volumes. We used the Brain Surface Extractor (BSE) [18] as a tool for skull stripping MRI images. As a first step, before using BSE, we processed the entire dataset using our super-resolution algorithm to enhance edges and anatomical boundaries. We then used BSE on the processed data set to obtain skull stripped versions of images. In order to test the accuracy of segmentation, we used an automated online resource (Segmentation, Validation Engine) [17] to test and evaluate segmentation algorithms. This system accepts a segmentation results (for e.g. running BSE on the entire data set after our algorithm) and compares it with the manually delinated, skull stripped intensity volumes already present in the LPBA 40 data set. It computes false positive and false negative values for each segmentation result, and colors the values at each voxel to obtain a projection map. Since the data volumes are initially processed in their native MRI space, we re-map the false positive and false negative results to a common atlas space based on the LPBA40 mappings. We then average these maps across the 40 subjects. For each cardinal direction (axial, sagittal, and coronal), we then sum the average counts along projections that are orthogonal to the plane of section. Table 1 shows the improvement in the results of skull stripping after the super-resolution algorithm is applied. In this table, the Jaccard similarity index, also known as the Tanimoto coefficient, measures the overlap of two sets. It is defined as the size of the intersection of the sets divided by the size of their union. The Dice coefficient represents the size of the union of 2 sets divided by the average size of the two sets. In both the cases, higher mean better.

Visually, these results are shown as colored average projection maps in Fig. 6. The first column shows the method and the measurement, for e.g. stdFP implies standard skull stripped, false positive, whereas SRFP implies super-resolved skull stripped false

positive. It is noticed that after super-resolution the average brightness intensity in all of the regions is reduced as compared to the standard result. This implies a lowering of the false positive rates, and improvement in segmentation.

Table 1. Comparison of Image metrics for skull stripped volumes before and after the application of the super-resolution algorithm.

Metric	Std	Edge
Dice coefficient	0.9316 ± 0.0305	0.9611 ± 0.0078
Jaccard index	0.8735 ± 0.0518	0.9253 ± 0.0144
Sensitivity	0.9868 ± 0.0055	0.9728 ± 0.0151
Specificity	0.9761 ± 0.0134	0.9909 ± 0.0039

5 Conclusion and Future Directions

We have presented a method for enhancement of resolution of images. The strengths of this approach lie in the i) TV norm as a regularizing functional in the variational model, and ii) a new piecewise-linear up(down) sampling operator that preserves edges. While we are aware that the proposed method works with the physical space, and not the frequency (k-space) of the data, we emphasize that the TV prior is a nonlinear prior that does modify the amplitudes of the k-space data. In other words, our algorithm works on the processed physical image, yet it modifies the spectral information implicitly in the data. This is an important point to be noted, especially in view of comparison with other methods that involve MRI image processing that work with the k-space representation of the data. We have demonstrated the improvement in spatial resolution for 2D as well as 3D anatomical MRI images. Furthermore we have also demonstrated its use as a preprocessing step for brain skull extraction from MRI images. The intuition in the improvement of skull stripped volumes after super-resolution processing stems from the fact that the total variation prior prefers edges, and tends to reduce uncertainty in their estimation. This implies that overall precision of the detection of edges will be improved by super-resolution. This translates in the lowering of the false positive rates and is evident from the experimental results. The edge-preserving operator maintains or sometimes even enhances edges in the image compared to other standard interpolation methods (including high order and sinc interpolation), whereas the Bregman iterations help in the recovery of higher order details from the image.

Diffusion Tensor Imaging (DTI) is an imaging modality that is gaining widespread attention due to its potential of imaging fiber tracts in the brain. However, the current acquisition resolution falls short of its intended use, viz. imaging the micro-structural information in the brain. One of the consequences of low resolution are artifacts such as PVE (partial volume effect), where a single imaged voxel may potentially contain multiple anatomical substructures or tissues. PVE can severely limit the analysis of directional and structural connectivity. In the future, we intend to investigate the effect of the proposed method to mitigate such issues.

Acknowledgments

This research was partially supported by the National Institute of Health through the NIH Roadmap for Medical Research, Grant U54 RR021813. Additionally, Dr. Antonio Marquina gratefully acknowledges the support from the NSF grants DMS-0312222, ACI-0321917, the NIH grant G54 RR021813, as well as DGICYT MTM2008-03597 from the Spanish Government Agency.

References

1. L. M. Bregman. The relaxation method of finding the common point of convex sets and its application to the solution of problems in convex programming. *USSR Comput. Math. and Math. Phys.*, 7:200–217, 1967.
2. D. Capel and A. Zisserman. Super-resolution from multiple views using learnt image models. *CVPR*, 2:627–634, 2001.
3. E. Carmi, S. Liu, N. Alon, A. Fiat, and D. Fiat. Resolution enhancement in MRI. *Magnetic Resonance Imaging*, 24(2):133–154, 2006.
4. S. Chaudhuri and M. Joshi. *Motion-Free Super-Resolution*. Springer-Verlag New York, Inc., 2005.
5. M. Elad and A. Feuer. Restoration of a single super-resolution image from several blurred,noisy, and undersampled measured images. *IEEE Tran. Image Processing*, 6(12):1646–1658, 97.
6. W. T. Freeman, T. R. Jones, and E. C. Pasztor. Example-based super-resolution. *IEEE Computer Graphics and Applications*, 22(2):56–65, 2002.
7. H. Greenspan, G. Oz, N. Kiryati, and S. Peled. MRI inter-slice reconstruction. *Magnetic Resonance Imaging*, 20:437 – 446, 2002.
8. M. Irani and S. Peleg. Improving resolution by image registration. *CVGIP: Graphical Models and Image Processing*, 53(3):231–239, 1991.
9. P. Kornprobst, R. Peeters, M. Nikolova, R. Deriche, M. Ng, and P. Van Hecke. A super-resolution framework for fMRI sequences and its impact on resulting activation maps. In *MICCAI*, pages 117–125, 2003.
10. F. Malgouyres. Total variation based oversampling of noisy images. In *Lect. Notes Comput. Sci.*, pages 111–122, 2001.
11. A. Marquina. Inverse scale space methods for blind deconvolution. *SIAM J. Imaging Science*, submitted.
12. A. Marquina and S. Osher. Image super-resolution by TV-regularization and Bregman iteration. *Journal of Scientific Computing*, doi:10.1007/s10915-008-9214-8, 2008.
13. F. Matteo and S. Johnson. The design and implementation of FFTW3. *Proceedings of the IEEE*, 93(2):216–231, 2005. special issue on "Program Generation, Optimization, and Platform Adaptation".
14. S. J. Osher, M. Burger, D. Goldfarb, J. Xu, and W. Yin. An iterative regularization method for Total Variation-based image restoration. *Multiscale Modeling and Simulation*, 4(2):460–489, 2005.
15. L. I. Rudin, S. Osher, and E. Fatemi. Nonlinear total variation based noise removal algorithms. *Physica D*, 60(1-4):259–268, 1992.
16. D. W. Shattuck, M. Mubeena, V. Adisetiyo, C., G. Salamon, K. L. Narr, R. A. Poldrack, R. M. Bilder, and A. W. Toga. Construction of a 3d probabilistic atlas of human cortical structures. *NeuroImage*, 39(3):1064–1080, 2008.
17. D. W. Shattuck, G. Prasad, M. Mirza, K. L. Narr, and A. W. Toga. Online resource for segmentation validation. *Neuroimage*, submitted.

18. D.W. Shattuck and R.M. Leahy. ”brainsuite: An automated cortical surface identification tool. *Medical Image Analysis*, 6(2):129–142, 2002.
19. H. Startk and P. Oskoui. High-resolution image recovery from image-plane arrays, using convex projections. *Journal of the Optical Society of America*, 6:1715–1726, 1989.
20. R. Y. Tsai and T. S. Huang. Multi-frame image restoration and registration. *Advances in Computer Vision and Image Processing*, pages 317–339, 1984.

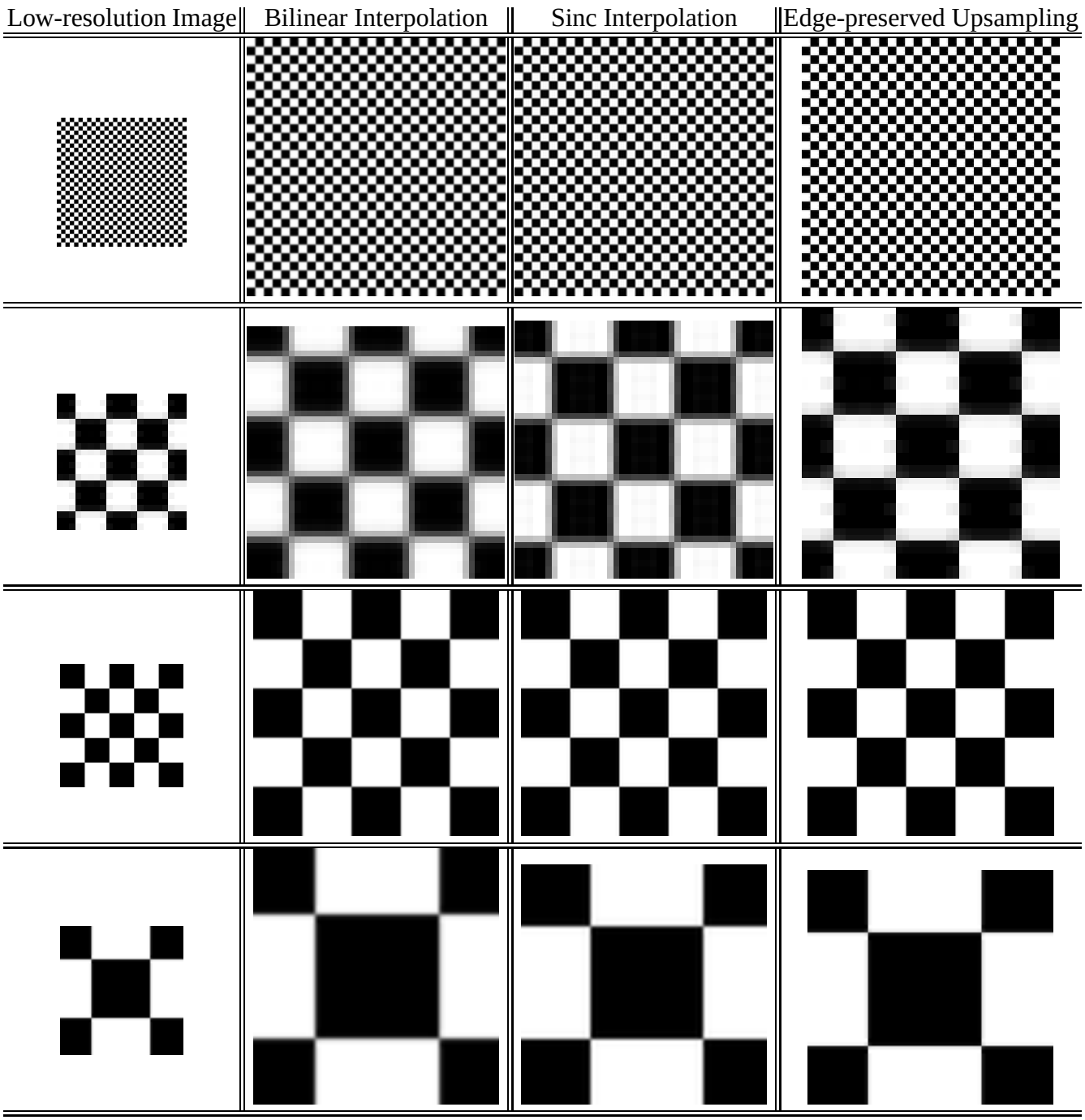

Fig. 1. The first and the third rows show a low-resolution image from the left, and its up sampled versions using a bilinear interpolation operator, a sinc operator, and the new edge-preserving operator for two different checkerboard patterns. The second and the third rows show a magnified area from the center of the image.

low-resolution image

bilinear interpolation

sinc interpolation

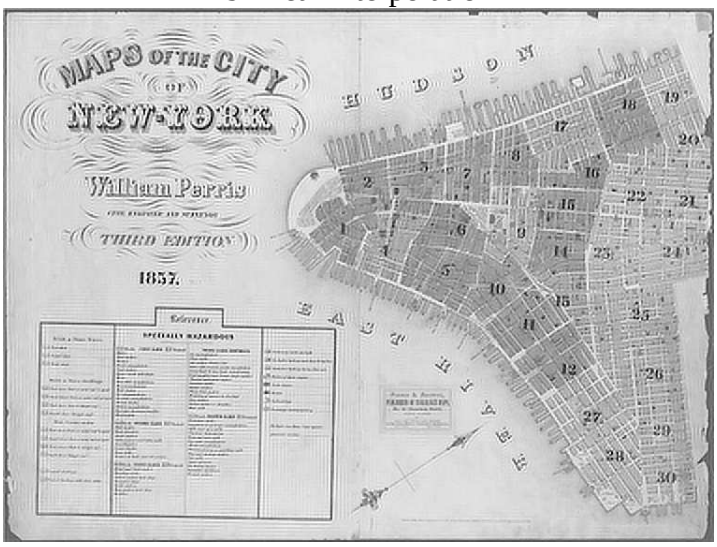

Super-resolved reconstruction

Fig. 2. Clockwise from top, a 380×285 low-resolution image, upsampled to twice the size by bilinear interpolation, sinc interpolation, and super-resolved reconstruction.

Fig. 3. Top row shows the low-resolution image, and the upsampled versions using bilinear, sinc and the super-resolved reconstruction. The bottom row shows a magnified detail of a portion of the image.

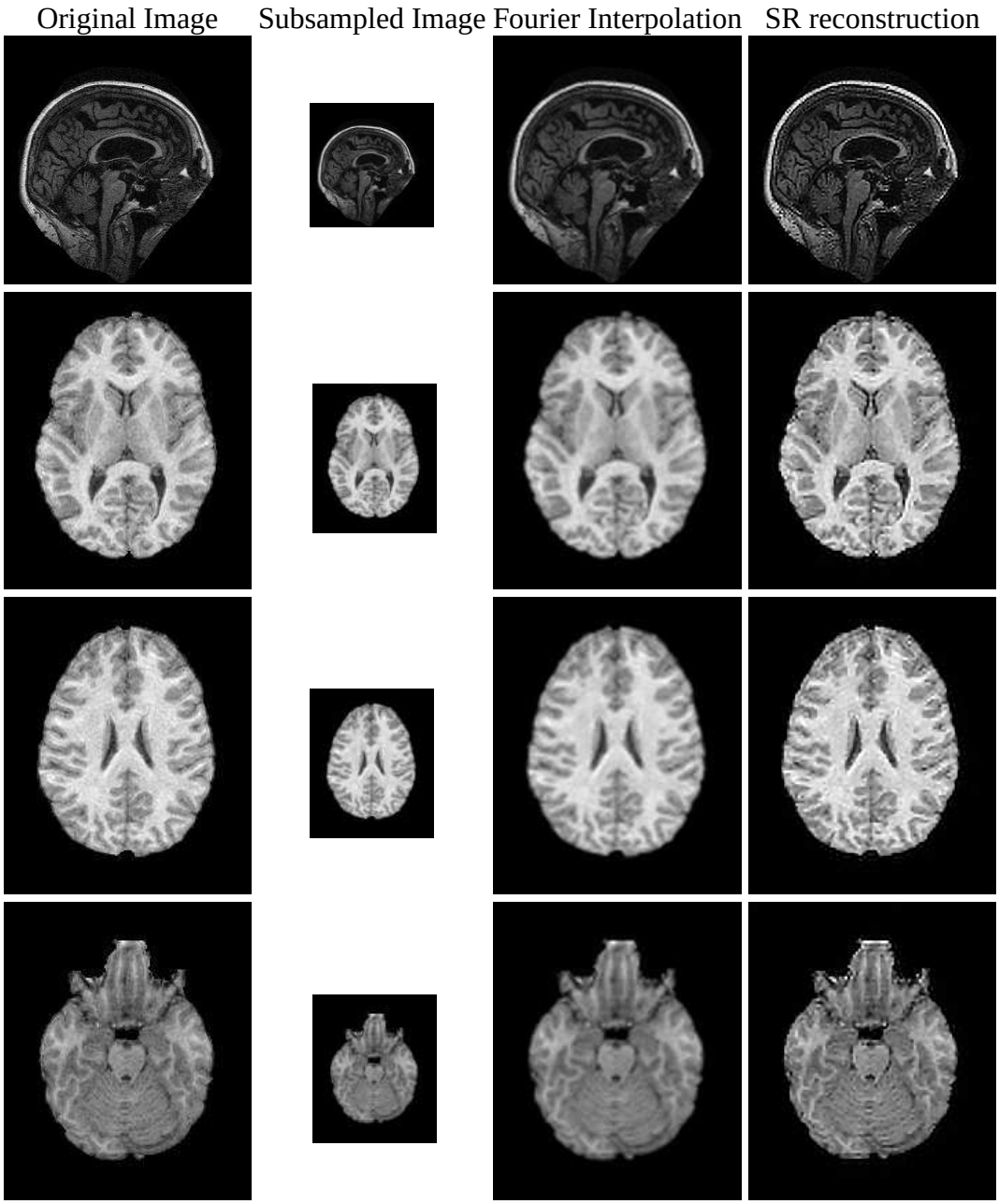

Fig. 4. Examples of super-resolved reconstruction for 2D slices of 3D MRI images.

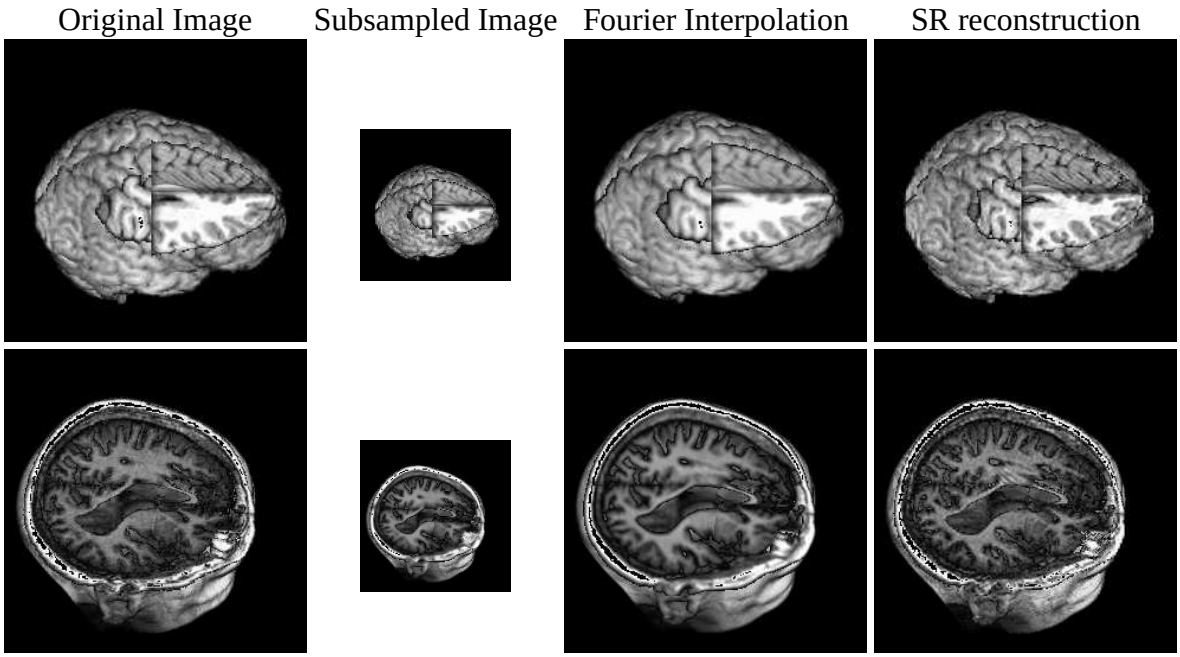

Fig. 5. Examples of super-resolved reconstruction for full 3D MRI images (volume rendered).

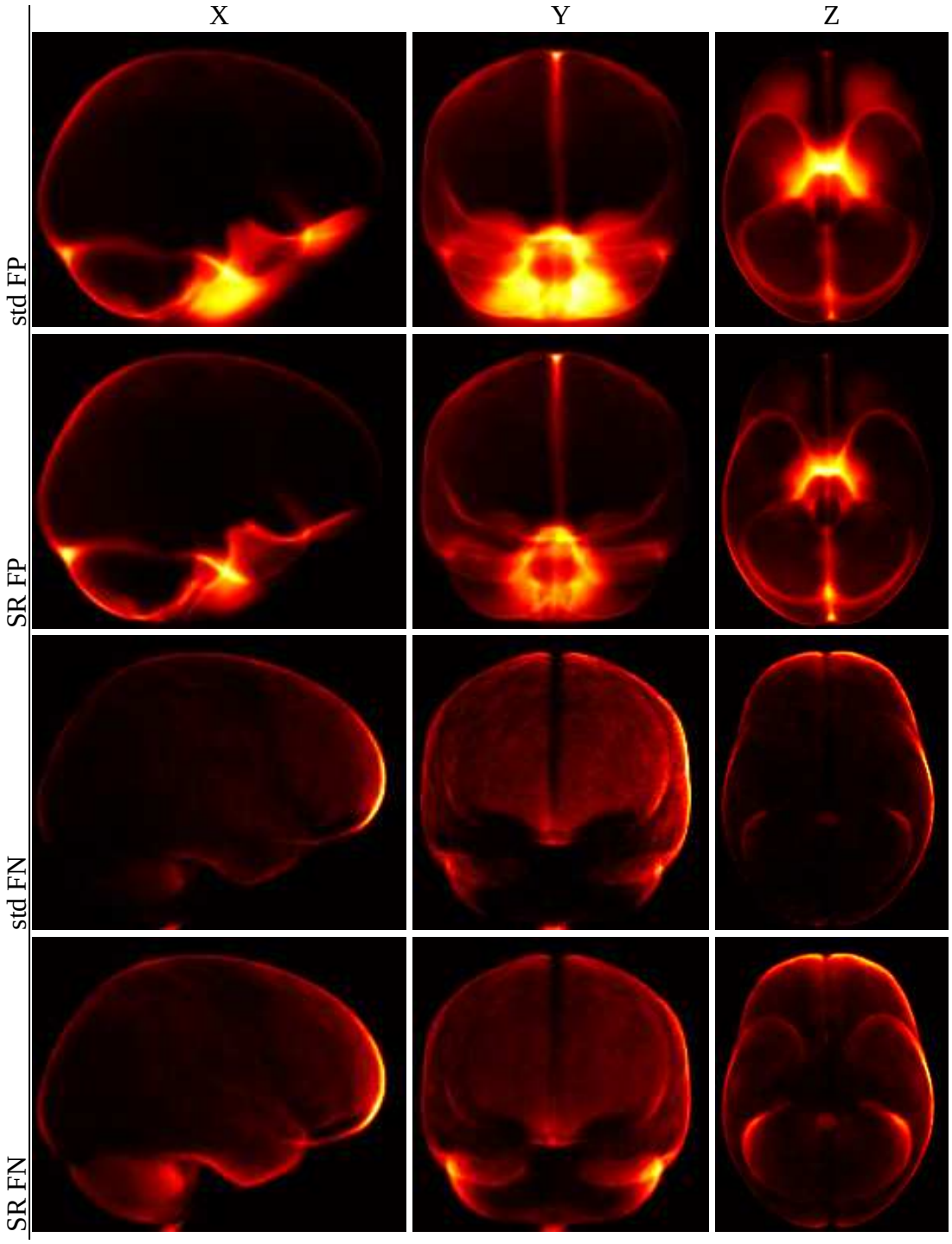

Fig. 6. Examples of projection maps for false positive and negative values for the segmentation result for each of the axial, sagittal, and coronal views.